Growing a 'cosmic beast': observations and simulations of MACS J0717.5+3745

M. Jauzac [1,2,3,4]★ D. Eckert,[5] M. Schaller [2] J. Schwinn [6] R. Massey [1,2]
Y. Bahé,[7,8] C. Baugh,[2] D. Barnes [9,10] C. Dalla Vecchia,[11,12] H. Ebeling,[13] D. Harvey,[4]
E. Jullo,[14] S. T. Kay,[9] J.-P. Kneib,[4,14] M. Limousin,[14] E. Medezinski,[15] P. Natarajan,[16]
M. Nonino,[17] A. Robertson [2] S. I. Tam[1] and K. Umetsu[18]

[1]*Centre for Extragalactic Astronomy, Department of Physics, Durham University, Durham DH1 3LE, UK*
[2]*Institute for Computational Cosmology, Durham University, South Road, Durham DH1 3LE, UK*
[3]*Astrophysics and Cosmology Research Unit, School of Mathematical Sciences, University of KwaZulu-Natal, Durban 4041, South Africa*
[4]*Laboratoire d'Astrophysique, Ecole Polytechnique Fédérale de Lausanne (EPFL), Observatoire de Sauverny, CH-1290 Versoix, Switzerland*
[5]*Max-Planck Institut für Extraterrestrische Physik, Giessenbachstrasse 1, D-85748 Garching, Germany*
[6]*Zentrum für Astronomie, Institut für Theoretische Astrophysik, Universität Heidelberg, Philosophenweg 12, D-69120 Heidelberg, Germany*
[7]*Leiden Observatory, Leiden University, PO Box 9513, NL-2300 RA Leiden, the Netherlands*
[8]*Max-Planck-Institut für Astrophysik, Karl-Schwarzschild Str. 1, D-85748 Garching, Germany*
[9]*Jodrell Bank Centre for Astrophysics, School of Physics and Astronomy, The University of Manchester, Manchester M13 9PL, UK*
[10]*Department of Physics, Kavli Institute for Astrophysics and Space Research, Massachusetts Institute of Technology, Cambridge, MA 02139, USA*
[11]*Instituto de Astrofísica de Canarias, C/Vía Láctea s/n, E-38205 La Laguna, Tenerife, Spain*
[12]*Departamento de Astrofísica, Universidad de La Laguna, Av. del Astrofísico Francisco Sánchez s/n, E-38206 La Laguna, Tenerife, Spain*
[13]*Institute for Astronomy, University of Hawaii, 2680 Woodlawn Drive, Honolulu, Hawaii 96822, USA*
[14]*Laboratoire d'Astrophysique de Marseille - LAM, Université d'Aix-Marseille & CNRS, UMR7326, 38 rue F. Joliot-Curie, 13388 Marseille Cedex 13, France*
[15]*Department of Astrophysical Sciences, 4 Ivy Lane, Princeton, NJ 08544, USA*
[16]*Department of Astronomy, Yale University, 260 Whitney Avenue, New Haven, CT 06511, USA*
[17]*INAF – Osservatorio Astronomico di Trieste, Via Tiepolo 11, I-34131 Trieste, Italy*
[18]*Institute of Astronomy and Astrophysics, Academia Sinica, PO Box 23-141, Taipei 10617, Taiwan*

ABSTRACT

We present a gravitational lensing and X-ray analysis of a massive galaxy cluster and its surroundings. The core of MACS J0717.5+3745 ($M(R < 1\,\mathrm{Mpc}) \sim 2 \times 10^{15}$ M$_\odot$, $z = 0.54$) is already known to contain four merging components. We show that this is surrounded by at least seven additional substructures with masses ranging $3.8-6.5 \times 10^{13}$ M$_\odot$, at projected radii 1.6–4.9 Mpc. We compare MACS J0717 to mock lensing and X-ray observations of similarly rich clusters in cosmological simulations. The low gas fraction of substructures predicted by simulations turns out to match our observed values of 1–4 per cent. Comparing our data to three similar simulated haloes, we infer a typical growth rate and substructure infall velocity. That suggests MACS J0717 could evolve into a system similar to, but more massive than, Abell 2744 by $z = 0.31$, and into a $\sim 10^{16}$ M$_\odot$ supercluster by $z = 0$. The radial distribution of infalling substructure suggests that merger events are strongly episodic; however, we find that the smooth accretion of surrounding material remains the main source of mass growth even for such massive clusters.

Key words: gravitational lensing – galaxy clusters: individual (MACSJ0717.5+3745) – dark matter – large-scale structure of Universe.

1 INTRODUCTION

Massive galaxy clusters are the most massive gravitationally bound structures in the present Universe, having grown by repeatedly accreting smaller clusters and groups (e.g. Fakhouri & Ma 2008; Genel et al. 2010). However, most of the mass in the Universe

is located outside gravitationally bound haloes. Clusters reside at the vertices of a cosmic network of large-scale filaments (Bond, Kofman & Pogosyan 1996). Numerical simulations predict these filaments contain as much as half of the Universe's baryons (Cen & Ostriker 1999; Davé et al. 2001) in the form of a warm plasma (Fang et al. 2002; Kaastra et al. 2006; Fang, Canizares & Yao 2007; Rasmussen 2007; Galeazzi, Gupta & Ursino 2009; Williams et al. 2010; Eckert et al. 2015), and the majority of the Universe's dark matter (Aragón-Calvo, van de Weygaert & Jones 2010).

Filaments are the scaffolding inside which clusters are built. They control the evolution of clusters. Particularly in the outskirts of a galaxy cluster, filaments create preferred directions for the accretion of smaller haloes, affecting the growth and shape of the main halo. Filaments also channel infalling galaxies, accelerating or 'preprocessing' their morphological and stellar evolution. Substructures in filaments bias cluster mass measurements, especially from weak gravitational lensing (Martinet et al. 2016). Mis-calibrating cluster number counts can bias cosmological constraints (Martinet et al. 2016), and mis-calibrating clusters' magnification of background galaxies can bias high-redshift galaxy number counts by up to 30 per cent (Acebron et al. 2017). For all these reasons, observationally assessing substructures is essential if cluster evolution is to be understood and exploited.

One of the most efficient ways of mapping a distribution of mass dominated by dark matter is gravitational lensing: the bending of light from a background source as it passes near a foreground mass (for reviews, see Massey et al. 2010; Kneib & Natarajan 2011; Hoekstra et al. 2013). Gravitational lensing is a purely geometrical effect, and is thus insensitive to the dynamical state of the cluster. It has been used extensively to probe the matter distribution in and around galaxy clusters (e.g. Kneib et al. 2003; Clowe, Gonzalez & Markevitch 2004; Bradac et al. 2006; Clowe et al. 2006; Limousin et al. 2007; Richard et al. 2011; Zitrin et al. 2011; Harvey et al. 2015; Massey et al. 2015; Jauzac et al. 2016; Natarajan et al. 2017; Chirivì et al. 2018). Additionally, observations of X-ray emission from infalling structures reveal the presence of hot gas – which, if virialized, is also an unambiguous signature of an underlying dark-matter halo (Neumann et al. 2001; Randall et al. 2008; Eckert et al. 2014, 2017; De Grandi et al. 2016; Ichinohe et al. 2015). The combination of lensing and X-ray information is thus a powerful tool to study the processes governing the growth of massive galaxy clusters.

The *Hubble Space Telescope* (*HST*) has recently obtained the deepest ever images of galaxy clusters, through the *Hubble Frontier Fields* (HFF) programme (Lotz et al. 2017). This targets six of the most massive clusters in the observable Universe, which we call 'cosmic beasts' because of their impressive size ($M_{200} \sim 10^{15}$ $M_\odot$). These objects are rare, but, as extrema, are also ideal tests of the cosmological paradigm.

One HFF galaxy cluster, Abell 2744, has been the source of recent debate. At redshift $z = 0.31$, it has a complex distribution of substructure in its core, and three filaments containing both dark matter and gas (Eckert et al. 2015). Jauzac et al. (2016) recorded a total of seven $> 5 \times 10^{13}$ $M_\odot$ mass substructures, projected within 1.2 Mpc of the cluster centre. Searching in the Illustris simulation volume (Vogelsberger et al. 2014), Natarajan et al. (2017) could not find a mass analogue to Abell 2744. However, performing zoom-in simulations they generated a comparable mass cluster and found good agreement between the lensing derived subhalo mass function determined from the Jauzac et al. (2015b) strong-lensing mass reconstruction and that derived from the simulated cluster across three decades in mass from 10^9 to $10^{12.5}$ $M_\odot$. Schwinn et al. (2017)

were unable to find any systems as rich in substructures in the entire Millenium-XXL (MXXL) simulation (Angulo et al. 2012). However, they suggested numerical and observational caveats to explain this apparent inconsistency: reduced resolution of the SUBFIND subhalo finder algorithm (Springel et al. 2001; Dolag et al. 2009) at lower density contrasts in the core of the main halo, comparison between 3D SUBFIND masses from simulations and 2D projected masses from lensing data, and the contamination of lensing masses by line-of-sight substructures. Mao et al. (2017) argued that as lensing measurements integrate mass along a line of sight, they include mass from additional structures, and quantified this effect using the Phoenix cluster simulations (Gao et al. 2012). The discrepancy might therefore be reduced by simulating observable quantities (Schwinn et al. 2018), or by simultaneously fitting all the components of a parametric mass model.

To obtain another example of the assembly of substructures; here, we study an even more massive HFF galaxy cluster, MACS J0717.5+3745 (MACS J0717), at higher redshift, $z = 0.54$. This is the most massive galaxy cluster known at $z > 0.5$ (Edge et al. 2003; Ebeling, Barrett & Donovan 2004; Ebeling et al. 2007), and one of the strongest gravitational lenses known (Diego et al. 2015; Limousin et al. 2016; Kawamata et al. 2016). Lensing and X-ray analyses of the cluster core have revealed a complex merging system involving four cluster-scale components (Ma, Ebeling & Barrett 2009; Zitrin et al. 2009; Limousin et al. 2012). A single filament extending south-east of the cluster core has been detected in the 3D distribution of galaxies (Ma et al. 2008) and the projected total mass from weak lensing (Jauzac et al. 2012; Medezinski et al. 2013; Martinet et al. 2016). We now exploit recent, deep observations from the *HST*, *Chandra X-ray Observatory*, *XMM–Newton X-ray Observatory*, Subaru, and Canada–France–Hawaii telescopes, to map the distribution of substructure up to ~5 Mpc from the cluster core in all directions, and to investigate the way the filament funnels matter into the centre. We then compare our results to theoretical predictions from the MXXL and Hydrangea/C-EAGLE (Bahé et al. 2017; Barnes et al. 2017b) simulations.

This paper is organized as follows. Section 2 presents the multiwavelength data sets used in our analysis. Section 3 presents the numerical simulations used in our comparison. Section 4 describes our gravitational lensing measurements, and Section 5 summarizes the technique we use to combine strong- and weak-lensing information. Section 6 compares our lensing results to the distribution of X-ray emitting gas. Section 7 discusses our findings in the context of theoretical predictions from numerical simulations. We conclude in Section 8. For geometric calculations, we assume a Λ cold dark matter (ΛCDM) cosmological model, with $\Omega_m = 0.3$, $\Omega_\Lambda = 0.7$, and Hubble constant $H_0 = 70$ km s^{-1} Mpc^{-1}. Thus, 1 Mpc at $z = 0.54$ subtends an angle on the sky of 2.62 arcsec, and at $z = 0.31$ subtends 3.66 arcsec. We quote all magnitudes in the AB system.

2 OBSERVATIONS

2.1 *HST* imaging

The core of MACS J0717 was initially imaged by *HST* as part of the X-ray-selected *MAssive Cluster Survey* (MACS; Ebeling, Edge & Henry 2001). Observations of 4.5 ks were obtained in each of F555W and F814W passbands of the *Advanced Camera for Surveys* (ACS; GO-09722 and GO-11560; PI: Ebeling). It was subsequently re-observed as part of the *Cluster Lensing And Supernovae with Hubble* survey (CLASH; GO-12066; PI: Postman; Postman et al. 2012), for an additional 20 orbits across 16

passbands from the UV to the near-infrared, with ACS and the *Wide-Field Camera 3* (WFC3). Finally, the strong lensing power of MACS J0717 made it an ideal target for the HFF observing campaign (Lotz et al. 2017). Its core was thus observed again for 140 orbits during Cycle 23, in 7 UV to near-infrared passbands, with ACS and WFC3 (GO-13498, PI: Lotz).

Meanwhile, a large-scale filament extending from the cluster core was discovered in photometric redshifts of surrounding galaxies from multicolour ground-based observations (Ebeling et al. 2004; Ma et al. 2009). This motivated mosaicked *HST*/ACS imaging of a $\sim 10 \times 20$ arcmin^2 region around the cluster in F606W and F814W passbands during 2005 (GO-10420; PI: Ebeling).

Data reduction of the core images used the standard HSTCAL procedures with the most recent calibration files (Lotz et al. 2017). ASTRODRIZZLE was used to co-add individual frames after selecting a common ACS reference image using TWEAKREG. The final stacked images have a pixel size of 0.03 arcsec. Data reduction of the mosaic observations is described in Jauzac et al. (2012). This followed a similar procedure as the core observations, except that exposures were treated independently to avoid resampling of the images that could affect weak-lensing shape measurements. These final images also have a pixel size of 0.03 arcsec.

2.2 Ground-based imaging

Wide-field imaging around MACS J0717 has been obtained from the 8.2 m Subaru telescope's SuprimeCam camera (34 arcmin × 27 arcmin field of view; Miyazaki et al. 2002) in B, V, R_c, I_c, and z' bands (Medezinski et al. 2013). The 3.6 m Canada–France–Hawaii Telescope (CFHT) has also obtained MegaPrime u^*-band imaging (1 deg^2 field of view) and WIRCam J and K_S-band imaging. All these data were reduced and analysed using standard techniques. For details, exposure times, and seeing conditions, we refer the reader to table 2 in Jauzac et al. (2012) and table 2 in Medezinski et al. (2013).

These ground-based observations were used for two purposes: (1) to measure photometric redshifts to remove contamination from both foreground and cluster galaxies to the weak-lensing catalogues; and (2) to measure the shapes of background galaxies outside the region observed by *HST*, for the wide-field weak-lensing analysis. Subaru weak-lensing measurements were obtained from the R_c-band image (see Section 4.3 for more details).

2.3 *Chandra* X-ray imaging

The *Chandra X-ray Observatory* has observed MACS J0717 on four occasions (OBSID 1655, 4200, 16235, and 16305), for a total exposure time of 243 ks. All observations were performed in ACIS-I mode. We reduced the data using CIAO v4.8 and CALDB v4.7.2. We used the `chandra_repro` pipeline to reprocess the event files with the appropriate calibration files and extracted source images in the [0.5–1.2] keV band using `fluximage`. We used the `blanksky` and `blanksky_image` tools to extract blank-sky data sets to model the local background, and we renormalized the blank-sky data such that the count rate in the [9.5–12] keV band matches the observed count rate to take the long-term variability of the particle background into account (Hickox & Markevitch 2006).

2.4 *XMM–Newton* X-ray imaging

XMM–Newton has observed MACS J0717 three times (OBSID 067240101, 067240201, 067240301, PI: Million) for a total ex-

posure time of 194 ks. We reduced the data using XMMSAS v15.0 and the corresponding calibration data base. We used the Extended Source Analysis Software (ESAS) package (Snowden et al. 2008) to analyse the data. We filtered the data for soft proton flares using the `pn-filter` and `mos-filter` tools, leading to a clean exposure time of 155 ks for MOS and 136 ks for pn. We extracted photon images in the [0.5–1.2] keV band for the three observations separately and used filter-wheel-closed data files to estimate the particle background contribution. Exposure times were computed using the XMMSAS tool `eexpmap`, taking the vignetting curve of the telescope and CCD gaps into account. The images of the three EPIC instruments were then combined and the various observations were mosaicked to create a total image of the cluster and its surroundings.

We also extracted spectra of several regions (see Section 6.2) to measure the thermodynamic properties of the gas. The spectra were extracted using the ESAS tasks `mos-spectra` and `pn-spectra`. Contaminating point sources were detected and excised using the `cheese` tool. Each background component was modelled separately and added to the total source model following the procedure described in Eckert et al. (2014). The background is split between the non-X-ray background, which we model using a phenomenological model tuned to describe the spectral shape of the filter-wheel-closed data, and the sky background. The latter can be described as the sum of three components: (i) an absorbed power law with a photon index of 1.46 to model the contribution of unresolved point-like sources (De Luca & Molendi 2004); (ii) an absorbed thin plasma model with a temperature of 0.22 keV to describe the X-ray emission of the Galactic halo (McCammon et al. 2002); (iii) a thin plasma model with a temperature of 0.11 keV to model the local hot bubble. We used a source-free region located ~ 10 arcmin northwest of the cluster core to estimate the relative intensity of the three sky background components. The measured normalizations were then rescaled to the area of the regions of interest. Finally, the source spectra were modelled as a single-temperature APEC model (Smith et al. 2001), leaving the temperature, emission measure and metal abundance as free parameters during the fitting procedure. For more details on the spectral modelling approach, we refer the reader to Eckert et al. (2014).

2.5 Spectroscopy and photometry

MACS J0717 has been extensively surveyed with the Deep Imaging Multi-Object Spectrograph (DEIMOS), the Low Resolution Imaging Spectrometer (LRIS), and Gemini Multi-Object Spectrograph (GMOS), on the Keck-II, Keck-I, and Gemini-North telescopes, respectively, on Mauna Kea. These observations (detailed in Ma et al. 2008 and summarized in Jauzac et al. 2012) cover both the core and the known filamentary structure. The DEIMOS instrument set-up combined the 600ZD grating with the GC455 order-blocking filter, with a central wavelength between 6300 and 7000. A total of 18 multiobject masks were observed with DEIMOS, with each of them having an exposure time of $\sim 3 \times 1800$ s, as well as 65 s and 48 s with LRIS and GMOS, respectively. These spectroscopic observations yielded redshifts of 1079 galaxies, 537 of which are confirmed as cluster members.

Ma et al. (2008) presented a photometric redshift catalogue for galaxies with $m_{R_C} < 24.0$, compiled using the adaptive SED-fitting code LE PHARE (Arnouts et al. 1999; Ilbert et al. 2006, 2009). We use this to calibrate colour–colour selections and to estimate the contamination from foreground and cluster galaxies in the weak lensing catalogues.

3 NUMERICAL SIMULATIONS

We use two state-of-the-art cosmological simulations to establish theoretical expectations and to interpret our observational results.

3.1 The MXXL dark matter simulation

The dark matter only MXXL simulation (Angulo et al. 2012) simulates the evolution of dark matter in a ΛCDM Universe ($H_0 = 100h = 73\,\mathrm{km\,s^{-1}\,Mpc^{-1}}$, $\Omega_\Lambda = 0.75$, $\Omega_\mathrm{m} = \Omega_\mathrm{dm} + \Omega_\mathrm{b} = 0.25$, $\Omega_\mathrm{b} = 0.045$, and $\sigma_8 = 0.9$). The dark matter fluid is traced by particles of mass $m_\mathrm{p} = 6.16 \times 10^9\,h^{-1}\,\mathrm{M_\odot}$ within a cube of volume $(3\,h^{-1}\,\mathrm{Gpc})^3$. Structures are detected within the MXXL simulation on two hierarchical levels. Dark matter haloes are found using the Friends-of-Friends (FoF) algorithm (Davis et al. 1985) using a linking length of $b = 0.2$. Within these FoF haloes, gravitationally bound subhaloes are identified using the SUBFIND algorithm (Springel et al. 2001; Dolag et al. 2009).

Schwinn et al. (2017) searched the MXXL for an analogue of galaxy cluster Abell 2744 ($z = 0.31$), which contains seven massive substructures at the cluster redshift plus one behind the cluster, within the central 2 Mpc (Jauzac et al. 2016). They found clusters as massive as Abell 2744, but none with as many substructures – at least not substructures detected by the FoF and SUBFIND algorithms. On the other hand, Natarajan et al. (2017) found good agreement with substructure in an Illustris zoom-in run with the strong-lensing derived substructure from the reconstruction of Jauzac et al. (2015b) between 10^9 and $10^{12.5}\,\mathrm{M_\odot}$. However, they were unable to match the radial distribution of the observed substructures and they reported an excess at the massive end that they attributed to systematics arising from the choice of SUBFIND as the halo finder.

However, further investigation using the particle data of the MXXL showed that this result seems to be caused by different definitions of a subhalo in the SUBFIND algorithm in comparison to the gravitational lensing analysis (Schwinn et al. 2018). Due to the immense amount of storage space needed, full MXXL particle data have only been stored for snapshots at $z = 3.06, 0.99, 0.24$, and 0. Here, our comparison of MACS J0717 relies on the closest MXXL snapshot at $z = 0.24$. As we will show, by analysing the particle data directly, we find two clusters with similar mass and a similar number of substructures (see Section 7.1 for details).

3.2 The Hydrangea/C-EAGLE hydrodynamical simulation

The Hydrangea/C-EAGLE suite of cluster simulations (Bahé et al. 2017; Barnes et al. 2017b) is a factor of a 1000 better in mass resolution than MXXL, and includes baryonic physics self-consistently. These 30 zoom-in simulations used the same physical model, resolution, and cosmology as the EAGLE simulations (Crain et al. 2015; Schaye et al. 2015), making this the largest sample of high-resolution clusters currently available. The clusters were selected from a parent dark matter only simulation of side-length 3.2 Gpc (Barnes et al. 2017a), using the ΛCDM cosmological parameters derived from the 2013 analysis of the *Planck* data (Planck Collaboration et al. 2014) ($H_0 = 100h = 67.77\,\mathrm{km\,s^{-1}\,Mpc^{-1}}$, $\Omega_\Lambda = 0.693$, $\Omega_\mathrm{m} = 0.307$, $\Omega_\mathrm{b} = 0.04825$, $\sigma_8 = 0.8288$, $n_s = 0.9611$, and $Y = 0.248$). As in the MXXL case, gravitationally bound haloes were found in the simulation using the FoF and SUBFIND algorithms. At $z = 0$, this simulation volume contains $>180\,000$ haloes with $M_{200} > 10^{14}\,\mathrm{M_\odot}$. Haloes that were not the most massive object within a radius of 30 Mpc or $20\,R_{200}$ (which ever is larger) around

their centre were removed from the sample, and 30 were selected for zoom-in re-simulation (see Bahé et al. 2017).

Higher resolution zoom-in initial conditions for each halo were then generated at $z = 127$ based on second-order perturbation theory following the method of Jenkins (2010). The initial particle masses were set to $m_\mathrm{DM} = 9.7 \times 10^6\,\mathrm{M_\odot}$ and $m_\mathrm{g} = 1.8 \times 10^6\,\mathrm{M_\odot}$ for the dark matter and gas, respectively. The Plummer-equivalent softening length was set to 0.7 kpc at $z < 2.8$ and is fixed in comoving space to 2.66 kpc at higher redshift.

The initial conditions were then run using the EAGLE simulation code (Crain et al. 2015; Schaye et al. 2015). The code is a highly modified version of the Tree-PM/SPH code GADGET (Springel 2005). The modifications to the hydrodynamics solver, including the use of the pressure–entropy formulation of SPH (Hopkins 2013), are described by Schaller et al. (2015) and the subgrid physics modules were designed and calibrated to reproduce the observed stellar mass function of galaxies at low redshift, yield galaxy sizes in agreement with low-redshift observations and a galaxy stellar mass – black hole mass relation compatible with observed data (Crain et al. 2015). The galaxy formation subgrid modules include metal-line cooling (Wiersma, Schaye & Smith 2009a) from an homogeneous Haardt & Madau (2001) X-ray/UV background radiation (with H reionization at $z = 11.5$), metallicity-dependent star formation (Schaye 2004; Schaye & Dalla Vecchia 2008), metal enrichment (Wiersma et al. 2009b), feedback from star formation (Dalla Vecchia & Schaye 2012), supermassive black-hole formation, and AGN feedback (Booth & Schaye 2009; Rosas-Guevara et al. 2015). Post-processed halo and subhalo catalogues have then been generated for all output redshifts using the SUBFIND algorithm. The $z = 0$ properties of these 30 haloes are given in appendix A1 of Bahé et al. (2017), whilst derived X-ray observable properties can be found in appendix A1 of Barnes et al. (2017b). All haloes were also simulated at the same resolution without baryonic processes.

4 GRAVITATIONAL LENSING MEASUREMENTS

4.1 Strong-lensing constraints

The deep HFF observations dramatically improved the strong-lensing mass model of the core of MACS J0717 (Zitrin et al. 2009; Limousin et al. 2012) thanks to the identification of more than 200 multiple images (Diego et al. 2015; Limousin et al. 2016; Kawamata et al. 2016). For this analysis, we use Limousin et al. (2016)'s mass model, which includes 51 multiple image systems (a total of 132 multiple images) to constrain the mass distribution of the cluster, 10 of which are spectroscopically confirmed. Ideally one would like a spectroscopic redshift confirmation for each systems, but this is unfortunately not possible as we do not have unlimited access to telescope time. However with MACS J0717, we are able to sample the redshift space behind the cluster thanks to the 10 systems with spectroscopic confirmation, thus decreasing the impact of the mass sheet degeneracy to the Limousin et al. (2016) model. Johnson & Sharon (2016) investigated the impact of the lack/abundance of spectroscopic redshifts on the resulting accuracy of the mass model and showed that at least a few multiple image systems with spectroscopic confirmations are crucial to produce a reasonable estimate of the mass (and the magnification). They also show that the availability of numerous (>15) spectroscopically confirmed multiple image systems increases the accuracy of the lens model without necessarily further improving the precision of the mass model. We refer the reader to the published work

by Johnson & Sharon ([2016](#)) for further details. The best-fitting mass model comprises four cluster-scale haloes, which are coincident with the four main light peaks, plus 90 galaxy-scale haloes in order to account for the impact of cluster galaxies on the geometry of nearby multiple images (Natarajan & Kneib [1997](#)). These galaxy-scale haloes correspond to cluster member galaxies identified with spectroscopic and photometric redshifts.

Limousin et al. ([2016](#)) presented two alternative strong-lensing mass models: one named *cored* that has a relatively flat distribution of mass in the smooth component and other named *non-cored* that results in a more 'peaky' mass distribution. Both models reproduce the geometry of the multiple images almost equally well, with an rms offset between observed and predicted positions of images of 1.9 arcsec and 2.4 arcsec for the *cored* and *non-cored* models, respectively. We tested both strong-lensing models in our strong+weak-lensing analysis. Both give similar results, as expected. However, for simplicity we shall only quote the combination of the *cored* strong-lensing mass model with our weak-lensing constraints in this paper.

4.2 *HST* weak-lensing catalogue

We note that we do not use HFF data for the weak-lensing analysis, as it only covers the core of MACS J0717 that is highly spatially extended and thus dominated by strong-lensing. Our *HST* weak-lensing analysis therefore relies on moderate depth *HST*/ACS imaging from the mosaic presented in Section 2.1. We measure the weak gravitational lensing shear signal from the shapes of galaxies in the ACS/F814W band. Our method is based on the *HST*/ACS lensing pipeline developed by Leauthaud et al. ([2007](#)) for COSMOS and adapted to galaxy clusters by Jauzac et al. ([2012](#)). This shear catalogue has already been published in Jauzac et al. ([2012](#)), so here we provide only a short summary of the procedures.

4.2.1 Background galaxy selection

We first detect sources using SEXTRACTOR (Bertin & Arnouts [1996](#)), employing the 'hot-cold' method (Rix et al. [2004](#); Leauthaud et al. [2007](#)) optimized for the detection of faint objects. This catalogue is then cleaned to remove spurious and duplicate detections. The star–galaxy classification is performed by looking at the distribution of sources in the magnitude (MAG_AUTO) versus peak surface brightness (MU_MAX) plane.

Only the images of galaxies behind the cluster have been gravitationally lensed by it. Foreground galaxies and cluster members must be removed from the shear catalogue, otherwise they will dilute the measured shear signal. For the 15 per cent of galaxies detected by *HST* that have spectroscopic or reliable photometric redshifts (Ebeling, Ma & Barrett [2014](#)), separating these galaxy populations is easy. For the remaining ∼85 per cent of galaxies, we apply a $(B - V)$ versus $(u - B)$ colour–colour selection, which is calibrated using the spectroscopic and photometric redshifts in the rest of the catalogue. Selection criteria for photometric redshifts and a detailed discussion of colour–colour selections and their calibration are provided in section 3.2 of Jauzac et al. ([2012](#)).

4.2.2 Galaxy shape measurements

We used the RRG moment-based shear measurement method (Rhodes, Refregier & Groth [2000](#)) to measure the shape of *HST*-detected background galaxies. This was specifically developed for space-based data with a small, diffraction-limited point spread function (PSF). It reduces noise by linearly correcting each shape moment for the effect of PSF convolution, and only dividing moments to compute an ellipticity at the very end. Both the size and the ellipticity of the ACS PSF vary considerably with time, due to 'breathing' of the telescope. Thermal fluctuations as parts of the telescope pass in and out of sunlight continually adjust its effective focus, thus making the PSF larger and more circular. To model the PSF, we used the grid of simulated PSF at varying focus offset created by Rhodes et al. ([2007](#)) using TINYTIM 6.3.

RRG returns a measure of each galaxy's apparent size, d, and apparent ellipticity, represented by a vector $\boldsymbol{e} = (e_1, e_2)$. From the latter, we obtain a shear estimator, $\tilde{\gamma} = C\boldsymbol{e}/G$, where G is the shear polarizability (which is computed from higher order shape moments of a large sample of galaxies), and $C = 1/0.86$ is a calibration factor computed by running the algorithm on mock *HST* data containing a known signal (Leauthaud et al. [2007](#)).

4.2.3 Catalogue cuts and weighting

We exclude from the catalogue any galaxies with shape parameters that our experience running the RRG algorithm on mock data suggests may be unduly noisy or biased. We keep only galaxies with detection significance signal-to-noise ratio (S/N) > 4.5; ellipticity $|\boldsymbol{e}| < 1$; and size $d > 0.13$ arcsec. Although ellipticity is by definition lower or equal to 1, RRG allows measured values greater than 1 because of noise. The restriction on the size of the galaxy is intended to eliminate sources with sizes approaching that of the PSF, thus making the shape of the galaxy difficult to measure.

Following Leauthaud et al. ([2010](#)), we also use an inverse-weighting scheme to optimize overall S/N from the remaining galaxies. We estimate the uncertainty in each shear estimator, $\sigma_{\tilde{\gamma}}$, by adding in quadrature intrinsic shape noise, σ_{int}, plus shape measurement error, σ_{meas}. We assume that intrinsic shape noise $\sigma_{\text{int}} = 0.27$ and errors on each ellipticity component are obtained by linearly propagating the covariance matrix of the moments (Leauthaud et al. [2010](#)). Weights $w_{\tilde{\gamma}} = 1/\sigma_{\tilde{\gamma}}^2$ then suitably down-weight the impact of noisy, faint galaxies.

In order to ensure unbiased measurements when combining strong- and weak-lensing information, we finally remove all galaxies located in the multiple-image region. Our final *HST* weak-lensing catalogue consists of 10 170 background galaxies, corresponding to a density of ∼52 galaxies per arcmin².

4.3 Subaru weak-lensing catalogue

In survey regions not covered by *HST* imaging, we measure the weak gravitational lensing shear signal from the shapes of galaxies in Subaru R_c-band imaging. Our shear catalogue has already been published in Medezinski et al. ([2013](#)), so here we provide only a short summary of the procedures.

4.3.1 Galaxy shape measurements

Our wide-field weak-lensing analysis uses the shape catalogue obtained by the CLASH collaboration (Postman et al. [2012](#)) from deep multiband Subaru/Suprime-Cam ($BVR_c i'z'$) and CFHT (MegaPrime $u*$ and WIRCam JK_S) observations. Full details of the image reduction, photometry, weak-lensing shape analysis, and background source selection are given in Medezinski et al. ([2013](#)) and Umetsu et al. ([2014](#)) (see their section 4 for more details on weak-lensing

systematics and see section 3 of Umetsu et al. 2016). Briefly summarizing, the weak-lensing analysis procedures include (1) object detection using the IMCAT peak finder (Kaiser, Squires & Broadhurst 1995), HFINDPEAKS, (2) careful close-pair rejection to reduce the crowding and deblending effects, and (3) shear calibration developed by Umetsu et al. (2010). For each galaxy, a shear calibration factor of 1/0.95 is included to account for the residual correction estimated using simulated Subaru/Suprime-Cam images (Umetsu et al. 2010). The CLASH Subaru shape measurements used the Suprime-Cam R_c data, which have the best image quality amongst the data in terms of the stability and coherence of the PSF-anisotropy pattern, and were taken in fairly good seeing conditions (0.79 arcsec in R_c; see table 2 of Medezinski et al. 2013).

4.3.2 Background galaxy selection

Following Medezinski et al. (2010), we identify background galaxies using a colour–colour selection in the $(B - R_c)$ versus $(R_c - z')$ plane calibrated with evolutionary tracks of galaxies [for more details see Medezinski et al. (2010) and Umetsu et al. (2010)] and the COSMOS deep photometric-redshift catalogue (Ilbert et al. 2009). Three samples are identified in this colour–colour space: red, blue, and green samples. The green sample encompasses mainly cluster members, and the red and blue ones two distinct lensed galaxy populations. While the red sample is limited to a magnitude mag$_{z'}$ < 25, the blue sample extends to fainter magnitude, mag$_{z'}$ < 26, as the number density of bluer galaxies grows significantly higher with magnitude. We adopt conservative colour limits in order to limit signal dilution due to the presence of cluster galaxies and foreground objects.

Our final Subaru weak-lensing catalogue consists of 4856 and 4738 galaxies in the red and blue lensed samples, respectively. This correspond to a density of 9.6 and 11.5 galaxies per arcmin^2 throughout the SuprimeCam field of view.

5 MASS MODELLING

5.1 Strong+weak lensing with Lenstool

The combination of strong- and weak-lensing constraints follows the methodology described in Jauzac et al. (2015a, 2016). We refer the reader to these publications for detailed discussions, and here only summarize the technique. It consists of combining both the parametric and the non-parametric approaches in the LENSTOOL software (Jullo et al. 2007, 2014; Jullo & Kneib 2009; Jauzac et al. 2012) in order to accommodate the high precision possible in the core thanks to strong-lensing constraints, while allowing more flexibility in the outskirts due to the lower information-density of the weak-lensing shear signal. We thus keep the strong-lensing parametric model described in Section 4.1 fixed to its best-fitting values, and add a multiscale grid of radial basis functions (RBFs) outside the cluster core to fit the weak-lensing constraints while optimizing the RBF amplitudes. Such an approach allows us to appropriately weight the strong-lensing constraints (see Jauzac et al. 2015a).

The parametric model is composed of four cluster-scale haloes (Limousin et al. 2016) to which we add 2244 pseudo-isothermal elliptical mass distribution potentials (PIEMD; Elíasdóttir et al. 2007) that represent the member galaxies, and a multi-scale grid of 2630 RBFs. Each RBF is modelled by a truncated isothermal sphere with core potential. Its position is fixed, and only its amplitude is allowed to vary over the optimization process. Its core

radius, s, is set to the distance to its closest neighbour, and its cut radius, t, is assumed to be $3 \times s$ (Jullo & Kneib 2009). The optimal solution we found consists of a multiscale grid composed of 2630 RBFs, with $s = 24$ arcsec for the smallest RBFs in regions with *HST* imaging (see Section 5.2): a maximum resolution similar to that obtained by Jauzac et al. (2012). Outside this field, where the density of background galaxies is the lowest due to the absence of high-resolution imaging from *HST*, the RBF core radii vary between $s = 192$ and 383 arcsec. Computational limitations currently prevent LENSTOOL from simultaneously optimizing the grid and the physical properties of individual cluster galaxies. The cut radius, ellipticity, and velocity dispersion of the galaxy-scale haloes are thus fixed to the values obtained by Limousin et al. (2016), and scaled from their luminosity in the K band (see Jauzac et al. 2012 for further details). These choices are considered reasonable as LENSTOOL was tested on simulated clusters and was found to perform successfully at constraining scaling-relation parameters for the overall cluster galaxy population (Meneghetti et al. 2017). Our team is working on overcoming those computational limitations and hopes to soon provide the community with an algorithm capable of fully optimizing all scales and lensing regimes with a non-parametric approach.

The contribution of the components of our model can be described as follows:

$$\tilde{\gamma} = M_{\gamma\nu}\nu + \gamma_{\text{param}} + \sigma_{\tilde{\gamma}} . \tag{1}$$

where the vector ν contains the amplitudes of the 2630 RBFs, the vector $\tilde{\gamma}$ is defined in Section 4.2 and contains the individual shape measurements of the background galaxies, and γ_{param} is the fixed ellipticity contribution from the strong-lensing parametric model. $\sigma_{\tilde{\gamma}}$ represents the noise as defined in Section 4.2. $M_{\gamma\nu}$ is the transformation matrix that contains the cross-contribution of each individual RBF to each individual weak-lensing galaxy. For the two shear components, we can write the elements of $M_{\gamma\nu}$ as

$$\Delta_1^{(j,i)} = \frac{D_{LSi}}{D_{OSi}} \Gamma_1^i(||\theta_i - \theta_j||, \ s_i, \ t_i), \tag{2}$$

$$\Delta_2^{(j,i)} = \frac{D_{LSi}}{D_{OSi}} \Gamma_2^i(||\theta_i - \theta_j||, \ s_i, \ t_i), \tag{3}$$

where Γ_1 and Γ_2 are given in Elíasdóttir et al. (2007, equation A8). Note that the shear in the cluster core can be large, and thus the assumption from equation (2) may not be strictly valid. However, the contribution to the grid-based model originates primarily from the weak-lensing regime as the cluster core contribution is accounted for mainly by the strong-lensing parametric model.

The parameter space is sampled using the MASSINF algorithm implemented in the Bayesys library (Skilling 1998) which is itself implemented in LENSTOOL (Jullo et al. 2007, 2014). At each iteration, the most significant RBFs are identified, and their amplitude is then adjusted to fit the ellipticity measurements. As an output, the algorithm gives us a large number of Markov chain Monte Carlo samples from which we can then derive mean values and errors on several quantities such as the mass density field and the magnification field amongst others.

Concerning the redshift of the background population, we follow the approach of Jauzac et al. (2015a, 2016). For background galaxies that do not have a spectroscopic redshift or a secure photometric redshift, we assume a redshift distribution described by $\mathcal{N}(z) \propto e^{-(z/z_0)^\beta}$, with $\beta = 1.84$ and a median redshift $\langle z \rangle = 1.586$ (Natarajan & Kneib 1997; Gilmore & Natarajan 2009). LENSTOOL requires each source to have its own redshift. Thus, the redshifts

for all galaxies without spectroscopic or photometric redshifts are randomly drawn from this distribution during the   initialization phase.

5.2 Grid resolution

Before converging on a grid of 2630 RBFs, we tested several possibilities including higher and lower resolution multiscale grids, as well as uniform grids. Our main goal is to study the distribution of substructure in the outskirts of MACS J0717, so we need to be careful to not introduce spurious substructures due to a high level of noise in the grid. A second point to consider is the different density of background galaxies resolved in the *HST* and Subaru weak-lensing catalogues.

A baseline for this study is provided by the analysis of Jauzac et al. (2012), which used *HST* weak-lensing data only. They tested the grid parameters, and converged on an optimal solution consisting of a multiscale grid with $s = 26$ arcsec for the smallest RBFs. For the present work to recover the filamentary structure with a similar significance level, we tried a uniform grid with a resolution of 24 arcsec. The motivation behind the uniformity of the grid is to avoid any prior on the mass distribution, such as that light traces mass. A uniform grid recovers the filament and all the substructures presented in Section 6.1. However, spurious detections are obtained due to a higher level of noise in the Subaru region as the resolution of the grid is too high compared to the density of weakly-lensed galaxies. Therefore, we tested a multiscale grid to account for the non-uniform background galaxy density. The optimal solution we found consists of a multiscale grid of 2630 RBFs, with the smallest RBFs having a core radius of $s = 24$ arcsec in the *HST* field of view, and with RBF core radii between $s = 192$ arcsec and $s = 383$ arcsec in the Subaru field of view. Our choice is conservative as we limit ourselves to the high-mass substructures, avoiding overextrapolation of the data that might lead to incorrect results.

6 RESULTS

6.1 Substructure detection from gravitational lensing

Our strong+weak lensing mass reconstruction of MACS J0717 reveals nine substructures located between 1.6 and 4.9 Mpc in projection from the cluster core (α: 109.39820; δ: 37.745778), which is itself composed of four merging clusters. Table 1 lists the substructures' and the cluster core (*Core*) coordinates, masses, and detection significance. All substructures are also highlighted in Fig. 2 with orange diamonds. We note that the large-scale filament detected in Jauzac et al. (2012) is not illustrated clearly in Fig. 2. The structure is detected with 3σ significance, a similar level as in Jauzac et al. (2012). However, we chose to draw contours that highlight the substructure detections, rather than the lower-density filament. Moreover, as a test of consistency between the Subaru and the *HST* weak-lensing analysis we compare the density profiles obtained in this region as shown in Fig. 1. Both profiles show a good agreement, with the Subaru one having larger error bars due to a much lower density of background galaxies.

The *Core* of MACS J0717 has been extensively studied due to its rich dynamical status, and therefore its lensing power. Its four main components are not the subject of this analysis, and are therefore all imbedded in the *Core* component (see Section 4.1). To test the reliability of our mass measurements, we first compare our mass values with published strong-lensing estimates from Limousin et al. (2016), Diego et al. (2015) and Kawamata et al. (2016).

For their *core* model, Limousin et al. (2016) measure a total mass of $M_{L16}(R < 990\,\text{kpc}) = (2.229 \pm 0.022) \times 10^{15}\,\text{M}_\odot$, which is in excellent agreement with our measurement, $M(R < 990\,\text{kpc}) = (2.214 \pm 0.050) \times 10^{15}\,\text{M}_\odot$. Diego et al. (2015) used a free-form method to build the strong-lensing mass model of MACS J0717 (WSLAP+, Diego et al. 2005, 2007; Ponente & Diego 2011; Lam et al. 2014; Sendra et al. 2014), and measured a mass of $M_{D15}(R < 80\,\text{kpc}) = 4.25 \times 10^{13}\,\text{M}_\odot$ (private communication), which is in excellent agreement with our mass estimate within the same aperture, $M(R < 80\,\text{kpc}) = (4.24 \pm 0.03) \times 10^{13}\,\text{M}_\odot$. Kawamata et al. (2016) used the parametric GLAFIC algorithm (Oguri 2010) and measured a total mass $M_{K16}(R < 80\,\text{kpc}) = 4.69 \times 10^{13}\,\text{M}_\odot$ (private communication). While their estimate is slightly higher than ours, it is of the same order.

We now discuss the several substructures detected on our strong- and weak-lensing mass map. SE1 and SE2 were previously detected in Jauzac et al. (2012), and as described in Section 6.2 both have an X-ray counterpart. They are also the most massive substructures found in MACS J0717 outskirts. The SE5, NE2, and SW2 substructures are all at the edge of the mass map. It is therefore difficult to disentangle between real substructures and artefacts from the mass modelling technique. Nevertheless, if they are real, the mass estimates should be taken with care. *NE2* is discussed in more detail in Section 6.2. Finally, SE1, SE2, SE3, SE4 (and possibly SE5) are all embedded in the large-scale filament identified in Jauzac et al. (2012). Moreover, all the detected substructures show an optical counterpart, and appear to be at the redshift of the cluster when identifying their galaxy counterparts using photometric and spectroscopic redshifts from Ma et al. (2008). NE1, NE2, and SE2 are all three detected by Durret et al. (2016). This double identification confirms all three are at the cluster's redshift, as Durret et al. (2016) detected them as overdensities of red-sequence galaxies.

6.2 X-ray and lensing properties of substructures

As already noted, MACS J0717 core has been extensively studied in the previous work (Ma et al. 2008; Mroczkowski et al. 2012; Adam et al. 2017a,b; van Weeren et al. 2017), and we thus refer the reader to these papers for a detailed analysis of the ongoing central merger. Here, we focus on the distribution of substructures in the surroundings of MACS J0717.
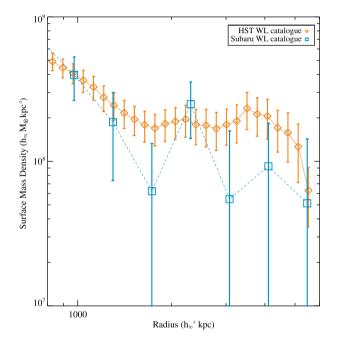
Amongst the nine substructures detected in the lensing map and listed in Table 1, two do not show a clear X-ray counterpart, SE3 and SE5. SE1 and SE2 are both detected in the X-ray, X1 and X2, respectively, in Table 2. Those massive X-ray groups were already known and highlighted in Jauzac et al. (2012). The alignment between X-ray and lensing peaks is almost perfect, leading to the conclusion that these two substructures are virialized, or falling in along the line of sight. SE3 is close to X3, a complex extended X-ray substructure. While its X-ray peak aligns really well with SE4, it is not clear that one of its components, north-west of X3, could not be associated with SE3. Indeed, this region of extended emission is apparently made of at least two and possibly three individual extended X-ray structures, as is shown by the cyan contours in Fig. 2. Moreover, this region is located at the edge of both the *XMM–Newton* and *Subaru* fields; thus, uncertainties in the position of the substructures are large. For these reasons, the association of SE3 with X3 is likely.

NE1 is associated with X6, and both peaks are well aligned. NE2 shows a bright X-ray counterpart, X4. While in Section 6.1, we warned the reader that *NE2* is located at the edge of the grid, the fact

Table 1. Coordinates, masses within 150 and 250 kpc apertures, significance of detection and projected distance to the cluster centre (D_{C-S}) for the substructures detected in the field of MACSJ0717. We take the *Core* coordinates as the one of the cluster itself following Limousin et al. (2016), located close to the centre of Group C (see their fig. 2).

ID	RA (deg)	Dec. (deg)	$M_{150}(10^{13}\,\mathrm{M_\odot})$	$M_{250}(10^{13}\,\mathrm{M_\odot})$	σ	$D_{C-S}(\mathrm{Mpc})$
Core	109.3982	37.745778	11.98 ± 0.11	30.78 ± 0.32	130	–
SW1	109.3087625	37.6497725	2.41 ± 0.59	6.19 ± 1.16	5	2.8
SW2[a]	109.3252847	37.54148293	1.34 ± 0.51	3.84 ± 1.38	3	4.9
SE1	109.4729667	37.70826611	2.28 ± 0.24	6.41 ± 0.62	10	1.6
SE2	109.58105	37.68432278	2.62 ± 0.60	6.51 ± 0.95	8	3.6
SE3	109.49475	37.61619444	2.20 ± 0.55	5.70 ± 1.31	5	3.5
SE4	109.5261625	37.59775361	1.85 ± 0.51	4.46 ± 0.97	4	4.1
SE5[a]	109.4714417	37.5501475	1.74 ± 0.54	4.72 ± 1.48	3	4.7
NE1	109.5142708	37.86093833	1.44 ± 0.46	4.18 ± 1.65	3	3.4
NE2[a]	109.6404125	37.84233667	2.27 ± 0.71	6.44 ± 2.00	3	4.9

[a]These substructures are located at the edge of the grid; therefore, their detection as well as their mass estimates should be taken with care.

Figure 1. Density profiles from the Subaru (cyan squares) and *HST* (orange diamonds) weak-lensing analysis along the large-scale filament detected by Jauzac et al. (2012).

that in the X-ray a similar structure is detected makes us confident in that detection. However, its lensing-mass estimate is biased by its proximity to the edge of the grid, and should thus be taken with care. SW1 is almost aligned with X5. This structure exhibits a flat and elongated X-ray morphology, which could indicate a previous interaction with the main halo. However, we caution that several X-ray bright foreground substructures (labelled as X9 and X10 in Fig. 2) are detected close to SW1 and may partly overlap with the X-ray emission associated with SW1/X5. Concerning SW2 and its X-ray counterpart, X7, both are located at the edge of the lensing grid and at the limit of the *XMM–Newton* imaging, similar to NE2 and X5. While NE2 appears quite massive both in the lensing and X-ray maps, SW2 is the least massive substructure in our sample. It is therefore particularly difficult to disentangle between a grid artefact/edge of *XMM–Newton* field of view and a real detection. Concerning SE5, as we explain in Section 6.1, it is located at the edge of the constrained region; therefore, it could reasonably be a

grid artefact, and it is also located at the edge of the *XMM–Newton* field of view. Therefore, we do not conclude on the existence of SE5. In comparison with NE2, which is clearly detected in both the lensing map and the X-ray map even if at the edge of the fields, SE5 is less massive.

In Table 2, we give the coordinates, the temperature, kT, the X-ray luminosity, and the gas mass within an aperture of 250 kpc, $L_{X,250}$, and $M_{gas,250}$, respectively, and for the X-ray remnant cores that have a correspondence with the lensing detections, their lensing ID, $S_{lensing}$, as well as their gas fraction, $f_{gas,250}$. We note that X8, X9, and X10 do not have any lensing counterparts. To identify these substructures, we used the NED catalogue and found a corresponding object for each of them. X8 is associated with a bright spiral galaxy, 2MASSX J07180932+3737031, which is a GALEX source for which we could not get any redshift. X9 is a well-known submillimetre galaxy (SMG) at $z = 0.06907$, 2MASSX J 07164427+3739556. Finally, X10 does not have any match in the NED catalogue; however, we suppose it is a foreground object as there is a bright galaxy at its position. Its proximity to X9 can lead to the assumption that it can be another foreground structure at a similar redshift as 2MASSX J07164427+3739556.

The gas fraction within a radius of $R < 250$ kpc for all substructures with a lensing counterpart varies between 1 per cent and 4 per cent. These relatively low gas fractions can be explained by two effects. First, each of these substructures are relatively low-mass/low-temperature groups within which we do not expect the total gas fraction to exceed 10 per cent (see fig. 20 in Vikhlinin et al. 2006 and fig. 4 in Eckert et al. 2016b). Secondly, the gas and lensing masses are measured in an aperture smaller than the virial radius of the structures, meaning that we could be missing some of the gas content and therefore we tend to underestimate the total gas fraction.

As a consistency check, we also look at the mass–temperature relation of these groups, and compare it with the Lieu et al. (2016) *M–T* relation, expressed as

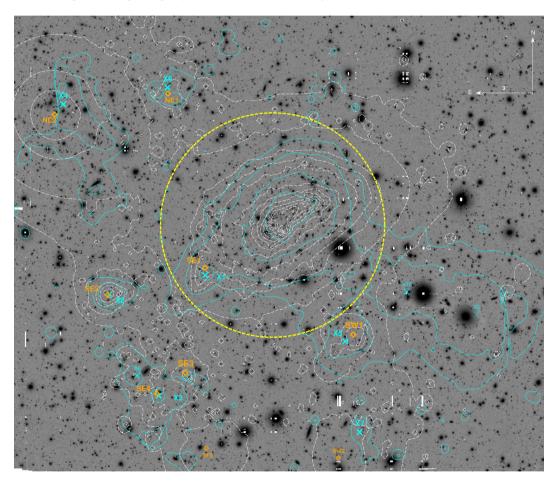$$\log \frac{E(z)M_{500,WL}}{h_{70}^{-1}\,\mathrm{M_\odot}} = a + b\log kT \qquad (4)$$

with $a = 13.57$ and $b = 1.67$, parameters derived from the XXL+COSMOS+CCCP sample. The $M_{500,WL}$ masses are estimated by fitting a NFW profile (Navarro, Frenk & White 1997) to the integrated mass profiles we obtain for each of the substructures (see Table 3). Such an estimate should be considered as an upper limit, as it will tend to overestimate the mass while converting 2D projected

Table 2. Coordinates, temperatures, X-ray luminosities in the [0.5–2] keV band, gas masses (within $\sim$250 kpc), and lensing counterpart (if any) of the infalling structures identified in our X-ray analysis.

ID	RA (deg)	Dec. (deg)	kT (keV)	$L_{X,250}$ (10^{42} erg s^{-1})	$M_{gas,250}$ (10^{11} M$_\odot$)	$S_{lensing}$	$f_{gas,250}$
X1	109.47288	37.701895	3.42 ± 0.18	23.0 ± 1.2	24.6 ± 1.0	SE1	0.04
X2	109.57894	37.685011	1.82 ± 0.26	10.7 ± 0.9	16.5 ± 1.3	SE2	0.03
X3	109.52414	37.596199	1.60 ± 0.29	11.0 ± 0.9	13.7 ± 1.8	SE4	0.03
X4	109.63088	37.851494	1.52 ± 0.16	18.0 ± 4.2	16.6 ± 3.5	NE2	0.03
X5	109.31781	37.643859	1.01 ± 0.11	5.6 ± 0.8	8.3 ± 3.2	SW1	0.01
X6	109.51502	37.866279	1.20 ± 0.16	11.2 ± 1.4	16.6 ± 3.5	NE1	0.04
X7	109.30196	37.564191	2.14 ± 1.17	6.7 ± 1.2	6.3 ± 3.3	SW2	0.02
X8[a]	109.54821	37.61343	–	–	–	–	–
X9[b]	109.17231	37.667292	–	–	–	–	–
X10[c]	109.24965	37.687168	–	–	–	–	–

[a]X8 corresponds to foreground spiral galaxy that we identified as 2MASSXJ 07180932+3737031.
[b]X9 corresponds to a well-known submilimetre galaxy, 2MASSXJ 07164427+3739556, at a redshift $z = 0.06907$.
[c]X10 location matches with a possible foreground galaxy; however, we could not find any redshift.

Figure 2. Subaru *R*-band image of MACS J0717. Orange diamonds highlight the position of substructures detected in the strong+weak lensing mass map (and listed in Table 1); cyan crosses highlight the positions of remnant cores detected in the *Chandra* and *XMM–Newton* maps. White contours show the mass distribution derived from our strong+weak lensing mass model; cyan contours represent the gas distribution deduced from *XMM–Newton* observations. The yellow circle has a radius of $R_{200} = 2.3$ Mpc (5.8 arcmin).

masses into 3D masses. Moreover, due to the fact that substructures cannot be isolated from each other, the mass of one may contribute to the integrated mass profile of another one. However, while our statistics is limited, we compare our results with the *M–T* relation measured by Lieu et al. (2016). One of the group falls right on the Lieu et al. (2016) relation, and the other lie above the relation by up to a factor of 2. This suggests that the M_{500} are overestimated.

7 COMPARISON OF SIMULATIONS AND OBSERVATIONS

Our goal is to observationally probe cluster evolution. MACS J0717 is a rare object due to its mass and dynamical state at $z = 0.54$. It is with such objects that we can test the limits of the cosmological paradigm. In two previous papers (Jauzac et al. 2016; Schwinn

Table 3. M_{500} estimates for the secured substructures detected in the field of MACSJ 0717.

ID	$M_{500}(10^{14} \, \mathrm{M_\odot})$
Core	4.03
SW1	1.90
SE1	2.01
SE2	2.07
SE3	1.68
SE4	1.16
NE1	1.05
NE2[a]	2.02

[a]NE2 is located at the edge of the grid; therefore, its mass estimate should be taken with care.

et al. 2017), we looked at a similar cluster, Abell 2744, at a lower redshift, $z = 0.31$. Abell 2744 has a similarly complex substructure distribution, including 7 substructures within ~ 2 Mpc of the cluster centre (plus one background substructure identified spectroscopically, a superposition along the line of sight). Additionally, three large-scale filaments extending out to ~ 7 Mpc that were detected by Eckert et al. (2015). Our present analysis also finds seven substructures around MACS J0717 (discarding the two being at the edge of the mass map and *XMM–Newton* field of view), but these are farther from the cluster centre: only one (SE1) is within 2 Mpc of the core, and the rest extend to ~ 5 Mpc.

Given the redshift, mass, and distribution of its substructure, we hypothesize that MACS J0717 is the progenitor of a structure that will look very similar to Abell 2744 by redshift $z = 0.31$. To test this hypothesis, we compare our observations of these two clusters with clusters in the numerical simulations MXXL (Angulo et al. 2012) and Hydrangea/C-EAGLE (Bahé et al. 2017, 2017b). We shall first check whether clusters as rich in substructure as MACS J0717 and Abell 2744 even exist in a ΛCDM model. Then we shall consider the mass growth rate and substructure infall rate of similar simulated clusters, in a way that is impossible in real systems that can be observed only in a snapshot at a single redshift.

7.1 Identification of simulated analogues

7.1.1 Comparison with MXXL

We use the two haloes with similar properties to Abell 2744 presented in Section 3.1 to investigate the infall of substructures into haloes. The reason for looking for Abell 2744 analogues rather than MACS J0717's is simply motivated by the lack of particle data output around $z = 0.54$ with MXXL. We only have particle data at $z = 0.24$, thus closer to Abell 2744's redshift. We therefore look for Abell 2744-like clusters (substructures close to the cluster's main halo) and trace them back in time using subhalo catalogues up to a redshift closer to MACS J0717's. *Cluster 1* has a mass of $M(R < 1.3 \, \mathrm{Mpc}) = 2.6 \times 10^{15} \, \mathrm{M_\odot}$ at $z = 0.24$ and the second cluster (*Cluster 2*) has a mass of $M(R < 1.3 \, \mathrm{Mpc}) = 2.5 \times 10^{15} \, \mathrm{M_\odot}$, both within the 3σ range of Abell 2744's mass. For both of these haloes, we create mass maps at $z = 0.24$ by projecting all particles over a distance of $30 \, h^{-1}$ cMpc on to a $5 \times 5 h^{-2}$ cMpc^2 map. Substructures within these haloes are then identified as overdensities within these maps and we check whether their mass within an aperture of 150 kpc lies within the 3σ interval of the masses obtained for Abell 2744 substructures.

None the less, as mentioned in Section 3.1, MXXL particle data are only available at a very small number of redshifts. If we want

Table 4. Evolution of radial distances in MXXL of SUBFIND-subhaloes for the snapshot closest to MACS J0717 redshift ($z \approx 0.56$) that closest to Abell 2744 redshift ($z \approx 0.28$) and that of the closest particle data output ($z \approx 0.24$). All distances are given as radial 2D distances from the position of the most massive subhalo in each snapshot in Mpc. The subhaloes denoted as SH1 are the central haloes.
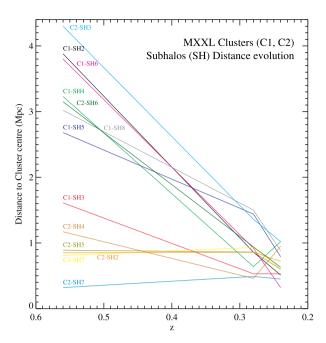
ID	$D_{z=0.56}$	$D_{z=0.28}$	$D_{z=0.24}$
Cluster 1–SH 1	0.00	0.00	0.00
Cluster 1–SH 2	3.88	0.86	0.51
Cluster 1–SH 3	1.61	0.53	0.53
Cluster 1–SH 4	3.23	0.64	1.02
Cluster 1–SH 5	2.68	1.44	0.79
Cluster 1–SH 6	3.80	0.92	0.32
Cluster 1–SH 7	0.81	0.93	0.60
Cluster 1–SH 8	3.02	1.50	0.88
Cluster 2–SH 1	0.00	0.00	0.00
Cluster 2–SH 2	0.85	0.86	0.72
Cluster 2–SH 3	4.30	1.36	1.02
Cluster 2–SH 4	1.17	0.46	0.95
Cluster 2–SH 5	0.89	0.86	0.60
Cluster 2–SH 6	3.15	0.94	0.63
Cluster 2–SH 7	0.32	0.49	0.45

Table 5. Evolution of masses of SUBFIND-subhaloes in MXXL for the snapshot closest to MACS J0717 redshift ($z \approx 0.56$) that closest to Abell 2744 redshift ($z \approx 0.28$) and that of the particle data ($z \approx 0.24$). The mass is given as the SUBFIND-mass, in units of $10^{14} \, \mathrm{M_\odot}$. The subhaloes denoted as SH1 are the central haloes.

ID	$M_{z=0.56}$	$M_{z=0.28}$	$M_{z=0.24}$
Cluster 1–SH 1	12.67	30.66	32.70
Cluster 1–SH 2	1.62	0.36	0.17
Cluster 1–SH 3	0.41	0.10	0.17
Cluster 1–SH 4	1.24	0.25	0.22
Cluster 1–SH 5	0.92	0.36	0.30
Cluster 1–SH 6	0.19	0.07	0.02
Cluster 1–SH 7	0.86	0.19	0.10
Cluster 1–SH 8	0.89	0.38	0.23
Cluster 2–SH 1	14.60	27.30	29.57
Cluster 2–SH 2	0.10	0.04	0.03
Cluster 2–SH 3	3.07	1.46	0.61
Cluster 2–SH 4	1.22	0.34	0.40
Cluster 2–SH 5	0.12	0.06	0.05
Cluster 2–SH 6	0.01	0.002	0.01
Cluster 2–SH 7	0.05	0.04	0.03

to analyse the evolution of the identified subhaloes up to $z = 0.55$ to compare with MACS J0717, we are dependent on the SUBFIND data sets of all other snapshots for which the particle data are not available. We thus identify the SUBFIND-subhaloes closest to the position of each subhalo identified in our projected mass map. We then use the merger trees available for each SUBFIND-subhalo in MXXL to trace the evolution of each subhalo back in time, at $z = 0.24$ (particle data), $z = 0.28$ and finally $z = 0.56$.

Table 4 lists the change in radial distances and Table 5 lists SUBFIND-masses of the Abell 2744-like substructures in both MXXL clusters. We list distances and masses at $z = 0.56$, corresponding to the snapshot closest to MACS J0717's redshift, at $z = 0.28$, the snapshot closest to Abell 2744's redshift, and then $z = 0.24$, the snapshot where particle data are available. For each subhalo, the radial 2D-distance projected along the line of sight and the SUBFIND-masses are given. The analysis of these two MXXL clus-

Figure 3. Projected distances to the main halo centre as a function of redshift for the two MXXL clusters' subhaloes as listed in Table 4.
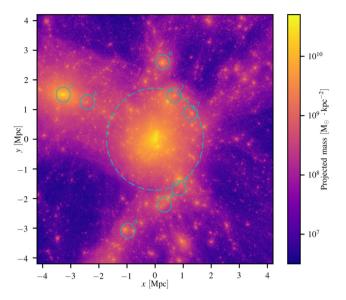

Figure 4. Projected mass map of halo CE-29 of the C-EAGLE simulation suite at $z = 0.47$ centred on the cluster's minimum of potential. At this time, the halo has a mass $M_{200} = 9.15 \times 10^{14}\,M_\odot$ and a spherical overdensity radius $R_{200} = 1.72$Mpc (dashed circle). The small cyan circles indicate the eight subhaloes that have a projected mass in a circular aperture of radius 250 kpc larger than our threshold for detection (see the text for details). The overall distribution of substructures is in qualitative agreement with what is observed in the MACSJ 0717 lensing mass map.

ters shows that subhaloes move by a distance of 2–3 Mpc between the redshifts of MACS J0717 and Abell 2744. While the subhaloes already close to the virial radius do not move much, the rest of the substructures get closer to the main halo centre by 2–3 Mpc. Fig. 3 shows the infalling distance of subhaloes as a function of redshift for *Clusters 1* and *2*.

The substructures that fall in from the furthest distances correspond mostly to the most massive substructures at redshift $z = 0.56$. During their infall their SUBFIND-masses decrease quite dramatically, in three cases by over 70 per cent. However, it is important to be very careful when comparing SUBFIND masses to aperture masses from gravitational lensing analysis. One reason for this discrepancy is that SUBFIND only assigns particles to a subhalo that are gravitationally bound to it. While this is a reasonable thing to do from a theoretical point of view, the substructures identified by this method are not easily comparable to those identified in gravitational lensing mass maps. In the latter, tidally stripped material and also the background halo contribute significantly to the subhalo masses (Mao et al. 2017). The degree of tidal stripping plays an important role here, which can be seen by the fact that the mass of three subhaloes drops by over 70 per cent (see Table 5). For a direct comparison of masses of simulated subhaloes to masses of observed subhaloes, it is much more reliable to obtain the subhalo 2D-projected masses from the simulation particle data if available.

Finally, we looked at the mass gain of the main haloes of *Cluster 1* and *Cluster 2* considering the evolution of M_{200} between $z = 0.56$ and $z = 0.28$. We measure a mass growth of $M_{C1,\,z=0.28}/M_{C1,\,z=0.56} = 3.7$ and $M_{C2,\,z=0.28}/M_{C2,\,z=0.56} = 1.9$. If we consider the mass growth between $z = 0.56$ and $z = 0.00$, we obtain $M_{C1,\,z=0.00}/M_{C1,\,z=0.56} = 4.0$ and $M_{C2,\,z=0.00}/M_{C2,\,z=0.56} = 2.5$.

7.1.2 Comparison with hydrangea/C-EAGLE

For the purpose of our comparison, we use the most massive halo (CE-29) present in the simulation. At $z = 0$, this cluster has a radius $R_{200} = 2.8$ Mpc, a mass $M_{200} = 2.4 \times 10^{15}\,M_\odot$, a soft X-

ray luminosity of $L_{500}^{0.5-2.0\text{keV}} = 8.8 \times 10^{44}\text{ergs}^{-1}$, a spectroscopic temperature $k_B T_{500} = 7.7$keV, and is the host of 826 galaxies with a stellar mass $> 10^9\,M_\odot$ (Bahé et al. 2017; Barnes et al. 2017b).

We analyse the snapshot of the simulation closest to the redshift of MACS J0717 at $z = 0.47$. We extract a cube of side-length 10 Mpc centred around the minimum of the potential of the halo. To construct a mass map, we project all the particles along the z-axis of the simulation volume and bin them using a regular grid with cells of side-length 2 kpc. The result of this procedure is shown in Fig. 4 with the dashed circle corresponding to the projected spherical overdensity radius $R_{200} = 1.72$ Mpc. Compared to actual weak-lensing data, this projected mass map is an idealized mass map, where any foreground and background structures perturbing the signal have been removed.

We then construct a catalogue of weak-lensing detected objects. We start by selecting all the haloes and subhaloes identified by the SUBFIND algorithm with a mass above $10^{10}\,M_\odot$ and compute the total projected mass in a 250 kpc circular aperture around their centre of potential. In a second step, we discard all such substructures with a projected mass under $10^{13}\,M_\odot$. This is slightly lower than the smallest object detected around MACS J0717 but is designed to allow for a systematical overestimation of the masses in the weak-lensing data. As pointed out by Schwinn et al. (2017) and more quantitatively by Mao et al. (2017), SUBFIND masses two orders of magnitude lower than a given aperture mass can be boosted by projection effects to reach the mass threshold. As we are aiming for a projected aperture mass of $10^{13}\,M_\odot$, our first selection of subhaloes with a SUBFIND mass above 10^{10} is justified. This procedure, however, does not guarantee that the structures analysed in this way would be detectable. An additional step to identify detectable overdensities is required. We hence iterate over all the substructures from the most massive to the least massive and eliminate the ones that overlap with a more massive object or that are within 1 Mpc of

Table 6. Projected mass ($M_{250,2D}$) within 250 kpc, hot gas mass ($M_{gas,250}$) within 250 kpc, projected distance (D_{2D}) to the cluster centre, velocity towards the centre of the halo (v_{centre}) and the fraction of gas ($f_{gas,250}$) for the eight objects selected via our mock weak-lensing analysis technique in the C-EAGLE cluster CE-29 at $z = 0.47$. The structure designated as SH1 is the main halo.

ID	$M_{250,2D}$ $(10^{13}\,M_\odot)$	$M_{gas,250}$ $(10^{11}\,M_\odot)$	D_{2D} (Mpc)	v_{centre} (km s^{-1})	$f_{gas,250}$
CE29–SH 1	20.1	59.8	0	0	0.03
CE29–SH 2	9.16	48.9	3.60	440	0.05
CE29–SH 3	1.64	0.9	1.63	−1100	0.01
CE29–SH 4	1.09	2.7	2.71	290	0.03
CE29–SH 5	1.02	0.4	1.87	300	0.004
CE29–SH 6	1.47	6.4	2.61	1070	0.04
CE29–SH 7	1.04	0.8	1.54	1290	0.01
CE29–SH 8	1.05	0.2	2.24	1280	0.002
CE29–SH 9	1.01	0.004	3.24	950	4.0×10^{-5}

Table 7. Masses of the C-EAGLE cluster CE-29 subhaloes at $z = 0.48$, 0.29, and 0.24. All masses are SUBFIND masses and are given in $M_\odot$. The structure designed as SH1 is the main halo.

ID	$M_{z=0.48}$	$M_{z=0.29}$	$M_{z=0.24}$
CE29–SH 1	9.15×10^{14}	9.76×10^{14}	10.70×10^{14}
CE29–SH 2	2.07×10^{14}	1.89×10^{14}	1.57×10^{14}
CE29–SH 3	1.68×10^{12}	1.37×10^{12}	1.32×10^{12}
CE29–SH 4	6.46×10^{11}	5.43×10^{11}	4.74×10^{11}
CE29–SH 5	5.55×10^{11}	4.56×10^{11}	4.55×10^{11}
CE29–SH 6	1.48×10^{13}	1.46×10^{9}	Merged
CE29–SH 7	4.23×10^{10}	2.82×10^{10}	1.63×10^{10}
CE29–SH 8	3.13×10^{11}	2.37×10^{11}	2.76×10^{11}
CE29–SH 9	3.13×10^{10}	3.22×10^{10}	1.19×10^{10}

the centre of the halo. This step is necessary as there is no way observationally to distinguish structures that overlap in projection. At the end of this procedure, we are left with eight subhaloes shown as small cyan circles on Fig. 4 with their masse, projected distance to the centre and velocity towards the centre of the cluster given in the first three columns of Table 6. The mass and distance range is similar to what we observe in MACS J0717. We also analysed the companion simulation without baryon physics and found projected masses in excellent agreement. This demonstrates that baryonic processes have little effects on these weak-lensing mass measurements.
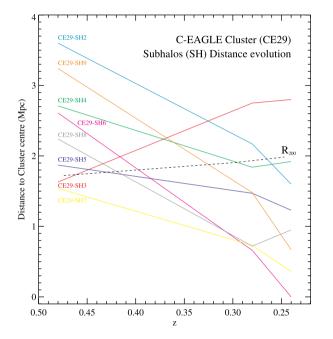
From the total masses of the halo (M_{200}), we can estimate a mass growth rate between $z = 0.47$ and $z = 0.29$ of $M_{z=0.47}/M_{z=0.29} = 1.20$. Moreover, between $z = 0.47$ and $z = 0.00$ we measure a mass growth rate $M_{z=0.47}/M_{z=0.00} = 2.62$. We note that CE-29 is undergoing a major merger at $z = 0.24$, which is responsible for such a high mass growth.

In Tables 7 and 8 we show the evolution of the projected distance of the subhaloes and their SUBFIND masses between $z = 0.47$ and $z = 0.24$. This is the closest we can get with available particle data to the respective redshifts of MACS J0717 and Abell 2744. As one can see in Fig. 5, they all have entered the virial radius region, except for CE29-SH3 that is a back-splash subhalo that will return towards the centre of the cluster at a later time. The average projected distance travelled to the main halo between $z = 0.47$ and $z = 0.24$ is in the range of 1–2 Mpc as can be seen in Fig. 5.

As discussed above, the SUBFIND masses cannot be related in a straightforward way to the projected mass within 250 kpc that can be observationally measured. Mao et al. (2017) showed that subhaloes

Table 8. Radial distances of the C-EAGLE cluster CE-29 subhaloes at $z = 0.47$, 0.30, and 0.25. All distances are given as radial 2D distances from the position of the main halo (SH1) in each snapshot in Mpc.

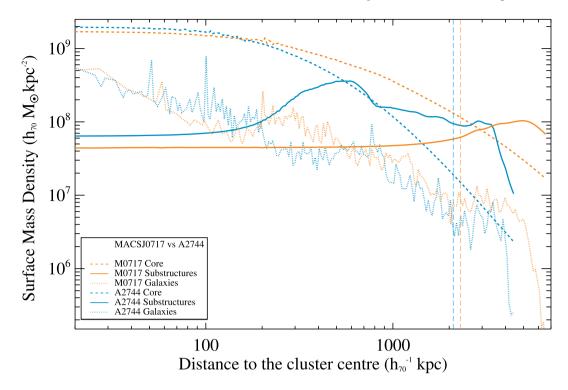| ID	$D_{z=0.47}$	$D_{z=0.30}$	$D_{z=0.25}$
CE29–SH 1	0.00	0.00	0.00
CE29–SH 2	3.60	2.17	1.60
CE29–SH 3	1.63	2.75	2.80
CE29–SH 4	2.71	1.84	1.92
CE29–SH 5	1.87	1.47	1.23
CE29–SH 6	2.61	0.66	0.00
CE29–SH 7	1.54	0.73	0.36
CE29–SH 8	2.24	0.72	0.95
CE29–SH 9	3.24	1.48	0.67

Figure 5. Projected distances to the main halo centre as a function of redshift for the C-EAGLE cluster' subhaloes as listed in Table 8. the black dashed line represents the evolution of R_{200}. As one can see, all substructures except for CE29-SH2 are within the virial region by $z = 0.24$.

embedded in a large halo can see their ratio of projected mass over SUBFIND mass reach values as large as 10^3. Similar boosts can also be seen in the substructures detected outside the virial radius but part of the larger overdensity around the cluster. This can be seen by comparing the masses reported in Tables 6 and 7.

7.2 Properties of a high-redshift supercluster

7.2.1 Infall of substructures

MACSJ 0717 substructures seem to be distributed along three preferred directions: south-east, north-east, and south-west, with neither lensing nor X-ray substructures detected in the north-west region as can be seen in Fig. 2. In the context of hierarchical structure formation scenarios, haloes are expected to be located at the intersection of three large-scale filaments (Bond et al. 1996), as was observed around Abell 2744 (Eckert et al. 2015). Nevertheless, all the dark matter substructures along with their X-ray counterparts, apart from the Core and SE1, appear to be located outside the virial radius of MACS J0717 (yellow circle on Fig. 2). However, Lau et al.

Figure 6. Density profile of the different components in MACS J0717 (orange) and Abell 2744 (cyan) as a function of the distance to the cluster centre: the core component (dashed line), the galaxy component (dotted lines), and the substructure component (plain lines). We differentiate between galaxies and (massive) substructures. The (long) dashed vertical lines highlight R_{200} for both clusters, MACS J0717 and Abell 2744, in orange and cyan, respectively.

(2015) show that up to $\sim 3 \times R_{200}$ (~ 7 Mpc), these substructures are already decoupled from the Hubble flow and therefore infalling into the cluster. Therefore, looking at both the dark and luminous mass distribution of MACS J0717, it is reasonable to assume that these detected substructures are falling into the cluster's main halo, and are doing so along three preferred directions, one of them at the location of which a dark matter large-scale filament was detected by Jauzac et al. (2012). However, only higher quality X-ray and weak-lensing data will enable us to confirm this assumption.

To start our investigation, we first estimate the distance that substructures like the ones observed here would travel within the redshift interval between MACS J0717 and Abell 2744. For this, we calculate the interval in look-back time, Δt_{lb}, for both cluster redshifts using the following expression:

$$t_{lb}(z) = t_H \int_0^z \frac{dz'}{(1 + z')} E(z'),\qquad(5)$$

where

$$E(z) = \sqrt{(\Omega_m(1 + z)^3 + \Omega_\Lambda)}\;.\qquad(6)$$

Applying equation (5) to the redshifts of Abell 2744 and MACS J0717, we obtain $t_{lb}(z = 0.31) = 3.4 \times 10^9$ yr and $t_{lb}(z = 0.54) = 5.3 \times 10^9$ yr. That gives us a look-back time $\Delta t_{lb} = 2.1 \times 10^9$ yr. If we make the hypothesis that the observed substructures in MACS J0717 are typical groups that have an infall velocity of ~ 1000 km s^{-1} (Lau et al. 2015), thus we estimate that between $z = 0.54$ and 0.31, the typical infall distance of substructures should be ~ 2 Mpc. This value is a lower limit estimate due to both projection effects and the fact that once substructures have entered the virial radius region, their infall velocity will increase as they are getting closer to the centre of the main halo.

Fig. 6 shows the density profiles of both MACS J0717 (orange) and Abell 2744 (cyan) as a function of the distance to the cluster centre for each of their components: the core of the cluster (dashed line), the substructure contribution (plain line) and the contribution from galaxies (dotted lines). We also highlight their respective R_{200} as vertical lines ($R_{200,0717} = 2.3$ Mpc; $R_{200,2744} = 2.1$ Mpc). From the core profiles, one can clearly see the different evolution stages between the two clusters: MACS J0717 has a slightly less dense but more extended core than Abell 2744, a typical signature of the change of the mass–concentration relation with redshift and mass. With time, substructures will infall and merge, the core density will increase and become more 'peaky' while leaving the outskirts of the cluster slightly under-dense as can be seen in Abell 2744. While substructures often refer to galaxies, we here refer to group to cluster-scale haloes ($M > 3.5 \times 10^{13}$ M$_\odot$). The substructure profiles in Fig. 6 clearly show the different evolutionary stages of the two clusters: the density of the substructure distribution peaks around ~ 5–6 Mpc in MACSJ 0717, and peaks at ~ 1 Mpc followed by a plateau up to 4.5 Mpc (limit of the field of view) in Abell 2744. This change of slope in Abell 2744 substructure's density profile is due to the presence of the large-scale filaments detected by Eckert et al. (2015). As a matter of consistency, we show all the clusters' components in Fig. 6. While the evolution stage of the object plays a key role in the shape of the density profiles of both the core and the substructure profiles, one can see that the galaxy density profiles for both clusters are similar and follow a similar slope. Applying our above infall distance estimate between $z = 0.54$ and $z = 0.31$ to MACS J0717 would mean that all the substructures would reach the virial radius by $z = 0.31$.

However, this analytic approach is limited. That is why we turn to numerical simulations such as MXXL (Angulo et al. 2012) and Hydrangea/C-EAGLE (Bahé et al. 2017; Barnes et al. 2017b) in

order to trace these 'independent' substructures (i.e. at $R > R_{200}$) between $z \sim 0.55$ and $z \sim 0.3$ and measure their average infall distance. In Abell 2744, all the substructures are detected within less than 2 Mpc from the core (excluding the filamentary structures outside R_{200}). Therefore, all substructures are assumed to be virialized within the main halo, which is not the case for MACS J0717. As explained at the beginning of this section, one motivation behind this analysis is to see if the assumption that MACS J0717 could be a progenitor of an Abell 2744-like cluster is realistic in terms of substructure infall and thus distribution. According to the calculation made earlier, it appears to be sensible (considering ~ 2 Mpc as a lower limit of infall distance between the redshift of the two clusters) to postulate that the actual substructures visible in MACS J0717 outskirts would have reached R_{200} by redshift $z = 0.31$, and is in good agreement with both MXXL and Hydrangea/C-EAGLE.

7.2.2 Mass growth rate

We now estimate the mass growth of MACS J0717. In order to estimate the growth due to substructure infall, we fit an NFW profile to all the secured substructures (see Section 6.2 and Table 3), i.e. excluding SE5 and SW2 from our calculations as well as SE1 which is already in the main halo ($D_{C–SE1} = 1.6$ Mpc). We can thus estimate a total mass of substructures $M_{500,Sub} = 0.98 \times 10^{15}$ M$_\odot$. Applying a similar fit to the Core component, we obtain a mass $M_{500,Core} = 4.03 \times 10^{15}$ M$_\odot$. Therefore, considering that all these substructures will be merging with the cluster main halo within R_{200} at $z = 0.31$, we can estimate that the mass growth of MACS J0717 due to massive substructures will be of a factor of 1.25 (over $\Delta t_{lb} = 2.1 \times 10^9$ yr).

When we compare the mass growth of MACS J0717 due to these substructures only we can see a good agreement with the mass growth estimated from Hydrangea/C-EAGLE ($M_{z=0.48}/M_{z=0.29} = 1.20$) and slightly lower than MXXL measurements ($M_{C1,\,z=0.28}/M_{C1,z=0.56} = 3.7$ and $M_{C2,\,z=0.28}/M_{C2,z=0.56} = 1.9$). Nevertheless, a few caveats have to be emphasized: (1) the MACS J0717 calculation relies on our conversion of aperture projected masses into M_{500}, and thus may lead to an overestimation of the mass growth rate, and (2) the growth rate relies on projected masses, however as shown by Mao et al. (2017) such masses can be overestimated by up to two orders of magnitude. Our relative agreement with numerical simulations could lead to the conclusion that the mass growth rate of these 'cosmic beasts' is not dominated by the smooth accretion of surrounding material (low mass substructures, i.e. not groups nor clusters), but rather by events of massive substructure infall. However, the true masses of the simulated substructures are given in Table 5 and Table 7. We note that the difference between those and their projected estimates can reach several order of magnitudes which is in agreement with Mao et al. (2017). That is suggesting that the majority of the mass growth measured for the simulated clusters is due to smooth accretion of low-mass substructures rather than infall of massive substructures.

MACS J0717 substructure distribution (up to $R \sim 5$ Mpc) and total mass leads us to the conclusion that we are observing a supercluster (Einasto et al. 2001, 2007; Chon, Böhringer & Nowak 2013), similar to what is observed in Pompei et al. (2016) at $z = 0.43$. If by $z = 0$ MACS J0717 has virialized, it will form an extremely massive cluster of $M_{200} \sim 10^{16}$ M$_\odot$ considering the average mass growth rate of 2.9 measured from both MXXL and C-EAGLE clusters. The clusters considered with MXXL and Hydrangea/C-EAGLE are the most massive objects visible in the simulations, and are all three

undergoing extreme merger events between $0.2 < z < 0.3$, making the average growth rate relatively large. However, considering the complexity of MACS J0717, we could expect it to undergo such an extreme dynamical history.

7.2.3 Gas fraction in substructures

Finally, we took advantage of the Hydrangea/C-EAGLE simulation that includes baryons in order to compare our measured gas fractions with the ones of the CE-29 substructures. The gas mass, $M_{gas,250}$, of each CE-29 substructures measured within an aperture of 250 kpc and the gas fraction, $f_{gas,250}$, are reported in Table 6. We here consider the hot gas mass in order to compare our results with what is measured in MACS J0717.

We measure relatively low gas fractions between 1 per cent and 5 per cent. This is in excellent agreement with MACS J0717 gas fractions as reported in Table 2. It confirms our initial hypothesis of an underestimated gas fraction due to a small aperture (not extending up to R_{200}), as well as the reliability of the baryonic physics in the Hydrangea/C-EAGLE suite of simulations.

8 CONCLUSIONS

The masses and distribution of substructures in the outskirts of massive galaxy clusters provide an observational test of the ΛCDM structure formation paradigm and at the same time present an opportunity to quantify the importance of major mergers in the build-up of these extreme objects. We have performed a combined strong-, weak-lensing, and X-ray analysis of observations from the *HST*, Subaru, *Chandra*, and *XMM–Newton* telescopes. We detected substructures in the outskirts of one of the most massive galaxy clusters in the observable Universe, MACS J0717 at $z = 0.54$, using the hybrid version of the LENSTOOL software (Jullo et al. 2007, 2010; Jauzac et al. 2012, 2015a). To interpret our findings, we have compared our observational results to our previous analysis of the massive cluster Abell 2744 at $z = 0.31$ (Jauzac et al. 2016) and two different cosmological simulations, MXXL (Angulo et al. 2012) and Hydrangea/C-EAGLE (Bahé et al. 2017; Barnes et al. 2017b).

Observational results: Our key observational results may be summarized as follows:

(i) We detect 9 group-scale substructures with masses ranging between $M(R < 250 \text{ kpc}) = 3.8$–$6.5 \times 10^{13}$ M$_\odot$ located between 1.6 and 4.9 Mpc from the cluster centre.

(ii) The X-ray analysis of the *XMM–Newton* and *Chandra* data reveals 10 substructures.

(iii) The combination with X-ray data allowed us to secure seven of the lensing detections.

(iv) The X-ray data show three substructures not detected in the lensing mass map (X8, X9, and X10) that we identified as being possible foreground objects in the NED catalogue.

(v) We measure the fraction of gas within a radius of 250 kpc, $f_{gas,250}$, for all substructures. $f_{gas,250}$ varies between 1 per cent and 4 per cent. This is well below the cosmic mean, in agreement with previous studies (Vikhlinin et al. 2006; Eckert et al. 2016a).

(vi) We look at the $M_{500,WL}$–T relation for these groups and compare our results with Lieu et al. (2016). This confirms the overestimation of our M_{500}.

Comparison with MXXL Hydrangea/C-EAGLE: Our key results from the comparison with numerical simulations can be summarized as follows:

(i) Clusters as rich in substructure as MACS J0717 and Abell 2744 are common in cosmological simulations, if the simulation data are analysed in a way compatible to the observations.

(ii) Projected mass maps of the two most massive clusters in the MXXL dark matter only simulation, and the most massive cluster in the hydrodynamical Hydrangea/C-EAGLE simulation (CE-29) all reveal a similar number of massive substructures as what is observed. The substructures in the latter also have hot gas fractions that are in excellent agreement with MACS J0717 (Figs 3–5).

(iii) From the total halo mass of the two MXXL clusters, we can estimate a mass growth rate of a factor of 3.7 and 1.9 for *Cluster 1* and *Cluster 2*, respectively, between $z = 0.56$ and 0.28, and of a factor of 4.0 and 2.5 between $z = 0.56$ and 0.00.

(iv) For the first time, we confronted theory and observations of gas fractions in massive galaxy clusters using state-of-the-art hydrodynamical simulations. We measured the gas fraction within an aperture of 250 kpc for each of CE-29 substructures, between 1 per cent and 5 per cent, which is in excellent agreement with what is observed in MACS J0717. From the evolution of the total halo mass in the Hydrangea/C-EAGLE cluster, M_{200}, we estimated a mass growth of a factor of 1.2 between $z = 0.48$ and 0.24.

Mass growth of MACS J0717: The substructure distribution in MACS J0717 is quite similar to what we observed in Abell 2744: seven substructures at the cluster redshift detected in both cases, with relatively lower masses in the case of MACS J0717 and more distant to the cluster centre. Such behaviour is expected while looking at the redshift difference between the two clusters, one being at a more advanced evolution stage than the other. Therefore, we ask ourselves the question of whether MACS J0717-like clusters could be the progenitors of Abell 2744-like clusters:

(i) A comparison between MACS J0717 and Abell 2744 suggests that the substructures we have identified in the former will move in towards the cluster centre by ∼2–3 Mpc between $z = 0.54$ and 0.31. This agrees with both analytic expectations and the radial motion of substructures in the simulations and suggests that MACS J0717 will, over time, evolve into a system similar to Abell 2744 in terms of substructure distribution.

(ii) Compared to Abell 2744, the core of MACS J0717 shows a more extended mass profile of its core and substructure components, while the mass profiles from their individual member galaxies agree well. We interpret this as evidence for a less evolved state of MACS J0717, as might be expected from its higher redshift and mass (Fig. 6).

(iii) From the lensing masses and expected infall velocity of the MACS J0717 substructures, we estimate a mass growth due to the accretion of massive substructures of a factor of 1.25 between $z = 0.54$ and 0.31, i.e. over a period of 2.1 Gyr. This is close to the total growth of the simulated cluster CE-29 over a similar redshift interval (1.20), but lower than the growth of either of the two MXXL clusters (3.7 and 1.9, respectively). Taking into account that our lensing-derived substructure masses are likely overestimated, this implies that the growth of 'cosmic beast' is dominated by the smooth accretion of surrounding material (low-mass substructures) rather than regular massive substructure infall events.

A supercluster at $z = 0.54$: MACS J0717 is a supercluster at $z = 0.54$ (Einasto et al. 2001, 2007; Chon et al. 2013; Pompei et al. 2016). Extrapolating its mass growth with expectations from simulations, it has likely evolved into an extremely massive cluster of $M_{200} \approx 10^{16}\,\mathrm{M_\odot}$ by the present day. We have shown that such massive systems are commonly surrounded by a large number of group-scale substructures, in agreement with recent observations at lower redshift (Haines et al. 2017) and cosmological simulations in a ΛCDM cosmology. Rather than constituting a challenge to our understanding of structure formation, our study has demonstrated that such objects offer a unique opportunity to directly observe the assembly of massive galaxy clusters. In the near future, we can hope to exploit this further by analysing the substructure content of other massive clusters, and extending it to protoclusters at higher redshift. Combined with cosmological simulations, such observations will enable a detailed probe of the assembly of 'cosmic beasts', the most massive bound structures in the Universe.

REFERENCES

Acebron A., Jullo E., Limousin M., Tilquin A., Giocoli C., Jauzac M., Mahler G., Richard J., 2017, MNRAS, 470, 1809

Adam R. et al., 2017a, A&A, 606, A64

Adam R. et al., 2017b, A&A, 598, A115

Angulo R. E., Springel V., White S. D. M., Jenkins A., Baugh C. M., Frenk C. S., 2012, MNRAS, 426, 2046

Aragón-Calvo M. A., van de Weygaert R., Jones B. J. T., 2010, MNRAS, 408, 2163

Arnouts S., Cristiani S., Moscardini L., Matarrese S., Lucchin F., Fontana A., Giallongo E., 1999, MNRAS, 310, 540

Bahé Y. M. et al., 2017, MNRAS, 470, 4186

Barnes D. J., Kay S. T., Henson M. A., McCarthy I. G., Schaye J., Jenkins A., 2017a, MNRAS, 465, 213

Barnes D. J. et al., 2017b, MNRAS, 471, 1088

Bertin E., Arnouts S., 1996, A&A, 117, 393

Bond J. R., Kofman L., Pogosyan D., 1996, Nature, 380, 603

Booth C. M., Schaye J., 2009, MNRAS, 398, 53

Bradac M. et al., 2006, A&A, 652, 937

Cen R., Ostriker J. P., 1999, ApJ, 519, L109

Chirivì G., Suyu S. H., Grillo C., Halkola A., Balestra I., Caminha G. B., Mercurio A., Rosati P., 2018, A&A, 614, A8

Chon G., Böhringer H., Nowak N., 2013, MNRAS, 429, 3272

Clowe D., Gonzalez A., Markevitch M., 2004, ApJ, 604, 596

Clowe D., Bradač M., Gonzalez A. H., Markevitch M., Randall S. W., Jones C., Zaritsky D., 2006, ApJ, 648, L109

Crain R. A. et al., 2015, MNRAS, 450, 1937

Dalla Vecchia C., Schaye J., 2012, MNRAS, 426, 140

Davé R. et al., 2001, ApJ, 552, 473

Davis M., Efstathiou G., Frenk C. S., White S. D. M., 1985, AJ, 292, 371

De Grandi S. et al., 2016, A&A, 592, A154

De Luca A., Molendi S., 2004, A&A, 419, 837

Diego J. M., Sandvik H. B., Protopapas P., Tegmark M., Benítez N., Broad-hurst T., 2005, MNRAS, 362, 1247

Diego J. M., Tegmark M., Protopapas P., Sandvik H. B., 2007, MNRAS, 375, 958

Diego J. M., Broadhurst T., Zitrin A., Lam D., Lim J., Ford H. C., Zheng W., 2015, MNRAS, 451, 3920

Dolag K., Borgani S., Murante G., Springel V., 2009, MNRAS, 399, 497

Durret F. et al., 2016, A&A, 588, A69

Ebeling H., Edge A. C., Henry J. P., 2001, ApJ, 553, 668

Ebeling H., Barrett E., Donovan D., 2004, ApJ, 609, L49

Ebeling H., Barrett E., Donovan D., Ma C.-J., Edge A. C., van Speybroeck L., 2007, ApJ, 661, L33

Ebeling H., Ma C.-J., Barrett E., 2014, ApJS, 211, 21

Eckert D. et al., 2014, A&A, 570, A119

Eckert D. et al., 2015, Nature, 528, 105

Eckert D., Jauzac M., Vazza F., Owers M., Kneib J.-P., Tchernin C., Intema H., Knowles K., 2016a, MNRAS, 461, 1302

Eckert D. et al., 2016b, A&A, 592, A12

Eckert D. et al., 2017, A&A, 605, A25

Edge A. C., Ebeling H., Bremer M., Röttgering H., van Haarlem M. P., Rengelink R., Courtney N. J. D., 2003, MNRAS, 339, 913

Einasto M., Einasto J., Tago E., Müller V., Andernach H., 2001, AJ, 122, 2222

Einasto M. et al., 2007, A&A, 476, 697

Elíasdóttir Á. et al., 2007, preprint (arXiv: 0710.5636)

Fakhouri O., Ma C.-P., 2008, MNRAS, 386, 577

Fang T., Marshall H. L., Lee J. C., Davis D. S., Canizares C. R., 2002, ApJ, 572, L127

Fang T., Canizares C. R., Yao Y., 2007, ApJ, 670, 992

Galeazzi M., Gupta A., Ursino E., 2009, ApJ, 695, 1127

Gao L., Navarro J. F., Frenk C. S., Jenkins A., Springel V., White S. D. M., 2012, MNRAS, 425, 2169

Genel S., Bouché N., Naab T., Sternberg A., Genzel R., 2010, ApJ, 719, 229

Gilmore J., Natarajan P., 2009, MNRAS, 396, 354

Haardt F. Madau P., Neumann D. M., Tran J. T. V., 2001, eds, Clusters of Galaxies and the High Redshift Universe Observed in X-rays

Haines C. P. et al., 2018, MNRAS, 477, 4931

Harvey D., Massey R., Kitching T., Taylor A., Tittley E., 2015, Science, 347, 1462

Hickox R. C., Markevitch M., 2006, ApJ, 645, 95

Hoekstra H., Bartelmann M., Dahle H., Israel H., Limousin M., Meneghetti M., 2013, Space Sci. Rev., 177, 75

Hopkins P. F., 2013, MNRAS, 428, 2840

Ichinohe Y., Werner N., Simionescu A., Allen S. W., Canning R. E. A., Ehlert S., Mernier F., Takahashi T., 2015, MNRAS, 448, 2971

Ilbert O. et al., 2006, A&A, 457, 841

Ilbert O. et al., 2009, ApJ, 690, 1236

Jauzac M. et al., 2012, MNRAS, 426, 3369

Jauzac M. et al., 2015a, MNRAS, 446, 4132

Jauzac M. et al., 2015b, MNRAS, 452, 1437

Jauzac M. et al., 2016, MNRAS, 463, 3876

Jenkins A., 2010, MNRAS, 403, 1859

Johnson T. L., Sharon K., 2016, ApJ, 832, 82

Jullo E., Kneib J., 2009, MNRAS, 395, 1319

Jullo E., Kneib J.-P., Limousin M., Elíasdóttir Á., Marshall P. J., Verdugo T., 2007, New Journal of Physics, 9, 447

Jullo E., Natarajan P., Kneib J.-P., D'Aloisio A., Limousin M., Richard J., Schimd C., 2010, Science, 329, 924

Jullo E., Pires S., Jauzac M., Kneib J.-P., 2014, MNRAS, 437, 3969

Kaastra J. S., Werner N., Herder J. W. A. d., Paerels F. B. S., de Plaa J., Rasmussen A. P., de Vries C. P., 2006, ApJ, 652, 189

Kaiser N., Squires G., Broadhurst T., 1995, ApJ, 449, 460

Kawamata R., Oguri M., Ishigaki M., Shimasaku K., Ouchi M., 2016, ApJ, 819, 114

Kneib J. et al., 2003, ApJ, 598, 804

Kneib J.-P., Natarajan P., 2011, A&AR, 19, 47

Lam D., Broadhurst T., Diego J. M., Lim J., Coe D., Ford H. C., Zheng W., 2014, ApJ, 797, 98

Lau E. T., Nagai D., Avestruz C., Nelson K., Vikhlinin A., 2015, ApJ, 806, 68

Leauthaud A. et al., 2007, ApJS, 172, 219

Leauthaud A. et al., 2010, ApJ, 709, 97

Lieu M. et al., 2016, A&A, 592, A4

Limousin M. et al., 2007, ApJ, 668, 643

Limousin M. et al., 2012, A&A, 544, A71

Limousin M. et al., 2016, A&A, 588, A99

Lotz J. M. et al., 2017, ApJ, 837, 97

Ma C.-J., Ebeling H., Donovan D., Barrett E., 2008, ApJ, 684, 160

Ma C.-J., Ebeling H., Barrett E., 2009, ApJ, 693, L56

Mao T.-X., Wang J., Frenk C. S., Gao L., Li R., Wang Q., 2018, MNRAS, 478, 34

Martinet N. et al., 2016, A&A, 590, A69

Massey R., Stoughton C., Leauthaud A., Rhodes J., Koekemoer A., Ellis R., Shaghoulian E., 2010, MNRAS, 401, 371

Massey R. et al., 2015, MNRAS, 449, 3393

McCammon D. et al., 2002, ApJ, 576, 188

Medezinski E., Broadhurst T., Umetsu K., Oguri M., Rephaeli Y., Benítez N., 2010, MNRAS, 405, 257

Medezinski E. et al., 2013, ApJ, 777, 43

Meneghetti M. et al., 2017, MNRAS, 472, 3177

Miyazaki S. et al., 2002, PASJ, 54, 833

Mroczkowski T. et al., 2012, ApJ, 761, 47

Natarajan P., Kneib J.-P., 1997, MNRAS, 287, 833

Natarajan P. et al., 2017, MNRAS, 468, 1962

Navarro J. F., Frenk C. S., White S. D. M., 1997, ApJ, 490, 493

Neumann D. M. et al., 2001, A&A, 365, L74

Oguri M., 2010, PASJ, 62, 1017

Planck Collaboration et al., 2014, A&A, 571, A16

Pompei E. et al., 2016, A&A, 592, A6

Ponente P. P., Diego J. M., 2011, A&A, 535, A119

Postman M. et al., 2012, ApJS, 199, 25

Randall S., Nulsen P., Forman W. R., Jones C., Machacek M., Murray S. S., Maughan B., 2008, ApJ, 688, 208

Rasmussen J., 2007, preprint (arXiv:0710.2531)

Rhodes J., Refregier A., Groth E. J., 2000, ApJ, 536, 79

Rhodes J. D. et al., 2007, ApJS, 172, 203

Richard J., Jones T., Ellis R., Stark D. P., Livermore R., Swinbank M., 2011, MNRAS, 413, 643

Rix H.-W. et al., 2004, ApJS, 152, 163

Rosas-Guevara Y. M. et al., 2015, MNRAS, 454, 1038

Schaller M., Dalla Vecchia C., Schaye J., Bower R. G., Theuns T., Crain R. A., Furlong M., McCarthy I. G., 2015, MNRAS, 454, 2277

Schaye J., 2004, ApJ, 609, 667

Schaye J., Dalla Vecchia C., 2008, MNRAS, 383, 1210

Schaye J. et al., 2015, MNRAS, 446, 521

Schwinn J., Jauzac M., Baugh C. M., Bartelmann M., Eckert D., Harvey D., Natarajan P., Massey R., 2017, MNRAS, 467, 2913

Schwinn J., Baugh C. M., Jauzac M., Bartelmann M., Eckert D., 2018, MNRAS, preprint (arXiv:1804.07401)

Sendra I., Diego J. M., Broadhurst T., Lazkoz R., 2014, MNRAS, 437, 2642

Skilling J., 1998, in Erickson G. J., Rychert J. T., Smith C. R., eds, Maximum Entropy and Bayesian Methods. p. 1

Smith R. K., Brickhouse N. S., Liedahl D. A., Raymond J. C., 2001, ApJ, 556, L91

Snowden S. L., Mushotzky R. F., Kuntz K. D., Davis D. S., 2008, A&A, 478, 615

Springel V., 2005, MNRAS, 364, 1105

Springel V., White S. D. M., Tormen G., Kauffmann G., 2001, MNRAS, 328, 726

Umetsu K., Medezinski E., Broadhurst T., Zitrin A., Okabe N., Hsieh B.-C., Molnar S. M., 2010, ApJ, 714, 1470

Umetsu K. et al., 2014, ApJ, 795, 163

Umetsu K., Zitrin A., Gruen D., Merten J., Donahue M., Postman M., 2016, ApJ, 821, 116

van Weeren R. J. et al., 2017, ApJ, 835, 197

Vikhlinin A., Kravtsov A., Forman W., Jones C., Markevitch M., Murray S. S., Van Speybroeck L., 2006, ApJ, 640, 691

Vogelsberger M. et al., 2014, MNRAS, 444, 1518

Wiersma R. P. C., Schaye J., Smith B. D., 2009a, MNRAS, 393, 99

Wiersma R. P. C., Schaye J., Theuns T., Dalla Vecchia C., Tornatore L., 2009b, MNRAS, 399, 574

Williams R. J., Mulchaey J. S., Kollmeier J. A., Cox T. J., 2010, ApJ, 724, L25

Zitrin A., Broadhurst T., Rephaeli Y., Sadeh S., 2009, ApJ, 707, L102

Zitrin A., Broadhurst T., Barkana R., Rephaeli Y., Benítez N., 2011, MNRAS, 410, 1939

This paper has been typeset from a TEX/LATEX file prepared by the author.